RIM-BP2 is required for rapid neurotransmitter release through regulation of Ca^{2+} channel clustering at hippocampal mossy fiber terminals.

Rinako Miyano[1], Hirokazu Sakamoto[2], Kenzo Hirose[2, 3], and Takeshi Sakaba[1]

[1]Graduate School of Brain Science, Doshisha University, Kyotanabe-shi, Kyoto 610-0394, Japan

[2]Department of Pharmacology, Graduate School of Medicine, The University of Tokyo, Bunkyo-ku, Tokyo 113-0033, Japan

[3]International Research Center for Neurointelligence (WPI-IRCN), The University of Tokyo, Bunkyo-ku, Tokyo 113-0033, Japan

Abstract

Synaptic vesicles dock and fuse at the presynaptic active zone (AZ), the specialized site for transmitter release. AZ proteins play multiple roles such as recruitment of Ca^{2+} channels as well as synaptic vesicle docking, priming and fusion. However, the precise role of each AZ protein type remains unknown. At phasic synapses having high release probability, Rab3-interacting molecule-binding protein2 (RIM-BP2) is known to affect Ca^{2+} channel localization at AZs. In order to dissect the role of RIM-BP2 at tonic synapses having low

release probability, we applied electrophysiological recording and super-resolution imaging to hippocampal mossy fiber terminals of RIM-BP2 KO mice. By using whole cell capacitance measurements, we found that reduced Ca^{2+} currents were responsible for the decreased rates of transmitter release in RIM-BP2 KO terminals. Consistently, STED microscopy pictured lower densities of P/Q-type Ca^{2+} channels at AZs deficient in RIM-BP2. Our results suggest that the RIM-BP2 function differs between phasic and tonic synapses.

Introduction

At chemical synapses, an action potential arriving at the presynaptic terminal opens voltage-gated Ca^{2+} channels, and Ca^{2+} influx through voltage-gated Ca^{2+} channels triggers neurotransmitter release from synaptic vesicles within ms. Synaptic vesicle fusion occurs at a specialized region of the presynaptic membrane called the active zone (AZ), where Ca^{2+} channel clusters and vesicle fusion sites are accommodated via AZ scaffold proteins (Südhof, 2012). For rapid transmission, accumulation of Ca^{2+} channels, co-localization of Ca^{2+} channels and fusion sites, and molecular priming of synaptic vesicles for fusion are required, and the differences between these factors might provide a basis for synaptic diversity. However, it remains unknown how these factors are regulated by AZ-scaffold proteins.

Rab3-interacting molecule-binding proteins (RIM-BPs) represent one principal,

37 conserved family of AZ proteins and bind to RIMs and Ca^{2+} channels (Wang et al., 2000;
38 Hibino et al., 2002). RIM-BP family includes RIM-BP1, RIM-BP2, and RIM-BP3 in mammals,
39 but RIM-BP3 expression is low in the nervous system (Mittelstaedt and Schoch, 2007). In
40 *Drosophila* neuromuscular junctions (NMJs), loss of RIM-BPs decreases Ca^{2+} channel
41 density and reduces release probability (Liu et al., 2011). Moreover, RIM-BP here is
42 necessary for tight coupling of synaptic vesicles to Ca^{2+} channels and replenishment of high
43 release probability vesicles at *Drosophila* NMJs (Liu et al., 2011; Müller et al., 2015, Petzoldt
44 et al., 2020). In mammalian synapses, the observations from KO mice are diverse. In RIM-
45 BP1,2 DKO mice, the coupling between Ca^{2+} channels and synaptic vesicles became loose,
46 and action potential-evoked neurotransmitter release was reduced at the calyx of Held
47 synapse (Acuna et al., 2015). At hippocampal CA3-CA1 synapses, RIM-BP2 deletion alters
48 Ca^{2+} channel localization at the AZs without altering total Ca^{2+} influx. Besides, RIM-BP1,2
49 DKO has no additional effect, indicating that RIM-BP2 dominates the function of RIM-BP
50 isoforms (Grauel et al., 2016). Tight coupling between Ca^{2+} channels and vesicles is crucial
51 for rapid and efficient transmitter release (Wadel et al., 2007).

52 In contrast, hippocampal mossy fiber-CA3 synapses are characterized by low
53 release probability (Vyleta and Jonas, 2014). At hippocampal mossy fiber synapses, gSTED
54 imaging suggested that RIM-BP2 KO altered the Munc13-1 cluster number and distribution.

55 In addition, RIM-BP2 deletion decreased the number of docked vesicles (Brockmann et al.,
56 2019). However, because of technically difficulty, direct and quantitative measurements of
57 exocytosis in RIM-BP2 KO terminals have not been performed so far.

58 To quantify the RIM-BP2 function in mossy fiber-CA3 synapses, we performed
59 whole-cell patch-clamp recordings from WT and RIM-BP2 KO hippocampal mossy fiber
60 boutons. We measured the size of the readily releasable pool (RRP) of synaptic vesicles,
61 Ca^{2+} influx, Ca^{2+} sensitivity of vesicle fusion, and the sensitivity of release to an intracellular
62 Ca^{2+} buffer. From electrophysiological recordings, we show that Ca^{2+} current amplitudes are
63 reduced in RIM-BP2 KO terminals, and that the reduction of Ca^{2+} currents is the dominant
64 factor for that of transmitter release. Using STED imaging, we find the densities of P/Q-type
65 Ca^{2+} channels in terminals to be reduced in RIM-BP2 KO. We suggest that RIM-BP2
66 regulates the number of P/Q-type Ca^{2+} channels at the AZ and is critical for rapid transmitter
67 release at hippocampal mossy fiber terminals.

68

69 **Results**

70 **RIM-BP2 KO reduces synaptic vesicle release and calcium currents at hippocampal**
71 **mossy fiber boutons.**

72 To investigate the roles of RIM-BP2 in synaptic transmission, we examined the

73 kinetics of exocytosis and Ca^{2+} influx in WT and RIM-BP2 KO synapses. We applied whole-
74 cell patch-clamp recordings and capacitance measurements to hippocampal mossy fiber
75 terminals in acute slices from WT and RIM-BP2 KO mice, in order to measure Ca^{2+} currents
76 and exocytosis directly. The patch pipette contained Cs^{+}-based internal solution and 0.5 mM
77 EGTA to isolate Ca^{2+} currents (Midorikawa and Sakaba, 2017). The external solution
78 contained 1 μM TTX to block Na^{+} currents. Membrane capacitance was measured by
79 applying a sinusoidal wave (1000 Hz, ±30 mV in amplitudes, Lindau and Neher, 1988). When
80 the terminal was depolarized from -80 mV to +10 mV for 10 ms, Ca^{2+} currents and membrane
81 capacitance were recorded as shown in Fig. 1A. During the depolarizing pulse, capacitance
82 was not measured due to large conductance changes, and the increase was used for
83 measuring synaptic vesicle exocytosis. To determine the size of the RRP and the time course
84 of exocytosis, we measured capacitance changes (ΔC_m) in response to various durations of
85 depolarization. Here, the length of the depolarizing pulse was varied between 5 ms and 100
86 ms, and ΔC_m plotted against pulse duration (Fig. 1B, bottom). ΔC_m in response to a 10 ms
87 pulse was reduced in RIM-BP2 KOs ($p = 0.0499$). ΔC_m became larger as the duration of
88 pulse was prolonged, but the increase started to be saturated at a 100 ms pulse in WT
89 terminals, suggesting depletion of the RRP. ΔC_m in response to a 100 ms pulse was 52 ± 9.1
90 fF ($n = 8$). The amplitude corresponds to the fusion of about 500-600 synaptic vesicles

91 (Hallermann et al., 2003; Midorikawa and Sakaba, 2017). The time course of ΔC_m could be
92 fitted by a single exponential with a time constant of 58 ± 11 ms. In RIM-BP2 KO terminals,
93 ΔC_m in response to a 100 ms pulse was smaller (41 ± 5.9 fF, n = 8) than that of WT terminals,
94 and the release time constant was slower (64 ± 14 ms) than in WT terminals. We should note
95 that the time constant is not necessarily reliable because the ΔC_m values do not reach a
96 plateau value at 100 ms pulse in some terminals. The amplitudes of Ca^{2+} currents were
97 smaller in RIM-BP2 KO terminals as compared to WT terminals (Fig. 1B, top). The Ca^{2+}
98 current in response to a 100 ms pulse was reduced by ~30% in RIM-BP2 KO terminals (27
99 ± 3.9 pA, n = 8) compared to WT terminals (41 ± 4.3 pA, n = 8) (p = 0.0379). Thus, the results
100 show that RIM-BP2 deletion reduces both neurotransmitter release and Ca^{2+} influx.

101 To investigate the Ca^{2+} influx in more detail, we examined the voltage dependence
102 of Ca^{2+} currents. Ca^{2+} currents were recorded in the presence of 1 μM TTX, a Na^+ channel
103 blocker, and 10 mM TEA, a K^+ channel blocker. Fig. 1C shows voltage step protocols and
104 representative current traces. Ca^{2+} currents were elicited by 5 ms depolarizing pulses from a
105 holding potential of -80 mV to various potentials to obtain I-V relationships. In both genotypes,
106 Ca^{2+} currents started to be activated at around -20 mV, and maximal amplitude was observed
107 at ~+10 mV (Fig. 1D). There was no major difference in the voltage dependence of Ca^{2+}
108 currents between WT and RIM-BP2 KO mice. Consistently, activation time constants of Ca^{2+}

109 currents were similar between WT and RIM-BP2 KO, when the terminal was depolarized to

110 +10 mV (τ = 1.4 ± 0.2 ms in WT, n = 6; τ = 1.3 ± 0.2 ms in KO, n = 4). These results suggest

111 a reduction in the number of Ca^{2+} channels rather than changes in activation kinetics is

112 responsible for the current decrease observed.

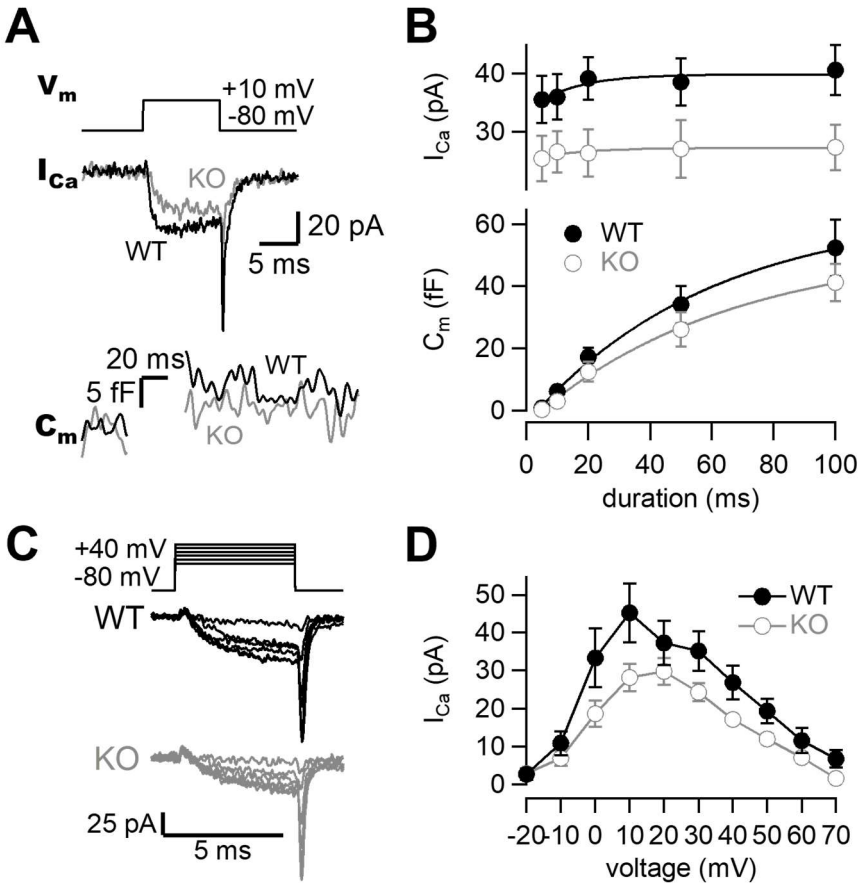

113

114 **Figure 1. RIM-BP2 KO reduces calcium currents and synaptic vesicle release**

115 (**A**) The terminal was depolarized from -80 mV to +10 mV in WT (black) and RIM-BP2 KO

116 (gray) hippocampal mossy fiber boutons. Ca^{2+} currents (I_{Ca}) and membrane capacitance (C_m)

117 in response to a 10 ms pulse (V_m) are shown. (**B**) *(top)* The peak Ca^{2+} currents were plotted

118 against the pulse duration. At 10 ms, p = 0.0499 (Wilcoxon rank sum test). *(bottom)* The
119 capacitance jumps were plotted against the pulse duration. At 20 and 100 ms, p = 0.0379
120 and 0.0379, respectively (Wilcoxon rank sum test). Black filled circles and gray open circles
121 represent the data from WT (n = 8) and RIM-BP2 KO (n = 8), respectively. Each data point
122 represents mean ± SEM. (**C**) Experimental protocol and representative traces for presynaptic
123 Ca^{2+} current measurements in WT (black) and RIM-BP2 KO (gray) boutons. Terminals were
124 sequentially depolarized for 5 ms with 2 ms intervals from -80 mV to +70 mV by 10 mV steps.
125 (**D**) Current-voltage relationships of peak Ca^{2+} currents in WT (black filled circle; n = 4-6) and
126 RIM-BP2 KO (gray open circle; n = 4-5). I_{Ca}s were elicited by 5 ms depolarizations. Each
127 data point represents mean ± SEM. Numerical values of plots are provided in Figure 1-source
128 data 1.
129 **Source data 1.** Datasets of Ca^{2+}-current and capacitance amplitudes presented in Figure 1.
130
131 **High extracellular calcium concentration rescues the decrease of synaptic vesicle**
132 **release in RIM-BP2 KO.**
133 Ca^{2+} influx controls exocytosis by regulating vesicular release probability and/or the
134 RRP size (Katz, 1969; Thanawala and Regehr, 2013). Because Ca^{2+} currents were reduced
135 in RIM-BP2 KO mice, we tested whether the reduction of release in RIM-BP2 KO mice could

136 be explained by that of Ca^{2+} influx or impaired synaptic vesicle docking / priming (Brockmann

137 et al., 2017). To increase Ca^{2+} influx, we raised the extracellular Ca^{2+} concentration ($[Ca^{2+}]_{ext}$)

138 from 2 mM to 4 mM. Ca^{2+} currents and membrane capacitances were recorded at 4 mM

139 $[Ca^{2+}]_{ext}$, and amplitudes then plotted against pulse duration (Fig. 2A). Although Ca^{2+} current

140 elicited by a 100 ms pulse in RIM-BP2 KO was still smaller (33 ± 2.7 pA, n = 3) than that in

141 WT (47 ± 6.6 pA, n = 4) (Fig. 2B, top), elevated $[Ca^{2+}]_{ext}$ increased Ca^{2+} currents in both WT

142 and RIM-BP2 KO mice. At 4 mM $[Ca^{2+}]_{ext}$, ΔC_m in response to a 100 ms pulse in RIM-BP2

143 KO was larger (51 ± 11 fF, n = 3) than at 2 mM $[Ca^{2+}]_{ext}$, and indeed showed a similar value

144 in WT at 2 mM $[Ca^{2+}]_{ext}$ (Fig. 2B, bottom). At the same time, ΔC_m in WT was not altered (53

145 ± 3.2 fF, n = 4) when higher $[Ca^{2+}]_{ext}$, suggesting that the RRP in WT was already depleted

146 at 2 mM $[Ca^{2+}]_{ext}$. Also, the time course of exocytosis at 4 mM $[Ca^{2+}]_{ext}$ was similar to that of

147 WT at 2 mM $[Ca^{2+}]_{ext}$, as the time courses were superimposable in Fig 2B. These results

148 suggest that a decrease in neurotransmitter release in RIM-BP2 KO could be rescued by an

149 increase in Ca^{2+} influx, easiest explained by a reduction of Ca^{2+} channel number.

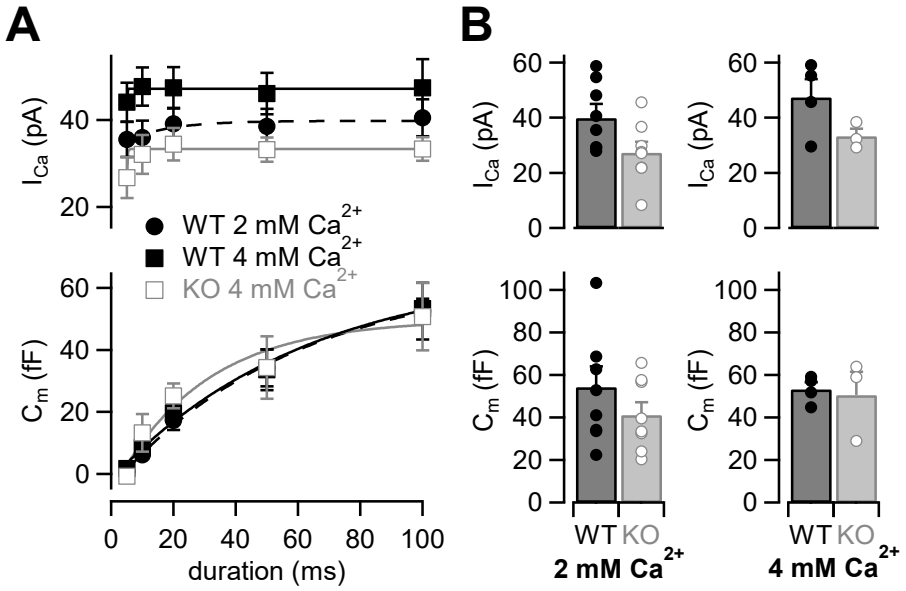

150

151 **Figure 2. High extracellular calcium concentration rescues the decrease of synaptic**

152 **vesicle release, but does not affect the RRP size**

153 (**A**) *(top)* The I_{Ca}s were plotted against the pulse duration in 4 mM $[Ca^{2+}]_{ext}$. *(bottom)* The C_ms

154 were plotted against the pulse duration in 4 mM $[Ca^{2+}]_{ext}$. Black filled squares and gray open

155 squares represent the data from WT (n = 4-6) and RIM-BP2 KO (n = 3-4), respectively. For

156 comparison, the WT data in 2mM $[Ca^{2+}]_{ext}$ are superimposed (black filled circle; n = 8) (the

157 same data set as Fig. 1B). Each data point represents mean ± SEM. (**B**) Average I_{Ca}s *(top)*

158 and C_ms *(bottom)* in response to a 100 ms pulse in WT (black bars) and RIM-BP2 KO (gray

159 bars) terminals. Extracellular Ca^{2+} concentration was 2 mM *(left)* or 4 mM *(right)*. Error bars

160 show SEM. Circles indicate individual values. Numerical values of plots are provided in

161 Figure 2-source data 1.

162 **Source data 1.** Datasets of Ca^{2+}-current and capacitance amplitudes presented in Figure 2.

163

164 **Decreased Calcium currents are mainly responsible for reduced release in RIM-BP2**

165 **KO.**

166 In order to further address whether the reduction of presynaptic Ca^{2+} influx observed

167 was responsible for the compromised release of RIM-BP2 KO mice, we adjusted Ca^{2+} current

168 amplitudes of WT to that of RIM-BP2 KO by lowering $[Ca^{2+}]_{ext}$. The amplitudes of Ca^{2+}

169 currents and capacitance jumps were plotted against pulse duration (Fig. 3A). At 1 mM

170 $[Ca^{2+}]_{ext}$, Ca^{2+} currents and ΔC_m were smaller than those of RIM-BP2 KO at 2 mM $[Ca^{2+}]_{ext}$.

171 At 1.5 mM $[Ca^{2+}]_{ext}$, Ca^{2+} currents became comparable to those of RIM-BP2 KO at 2 mM

172 $[Ca^{2+}]_{ext}$. Here, the ΔC_m evoked by a 100 ms pulse (43 ± 6.7 fF, n = 5) was comparable

173 between WT and RIM-BP2 KO (Fig 3A). The average time course of capacitance increase

174 of WT at 1.5 mM $[Ca^{2+}]_{ext}$ was similar to that of RIM-BP2 KO at 2 mM $[Ca^{2+}]_{ext}$. Therefore, by

175 reducing Ca^{2+} currents, WT data could reproduce the release time course of RIM-BP2 KO.

176 In Fig. 3B, ΔC_m in response to a 100 ms pulse at various $[Ca^{2+}]_{ext}$s were plotted against the

177 peak Ca^{2+} current amplitudes. The relationship could be fitted by a Hill plot with n = 3 in WT

178 (Schneggenburger et al., 1999). Consistently, when capacitance jumps elicited by various

179 pulse durations are plotted against total Ca^{2+} influx (Fig. S1), the RIM-BP2 KO data were

180 superimposed on the WT data, indicating that Ca^{2+}-sensitivity for release was not altered and

181 that the reduction of Ca^{2+} currents determine the reduced release in RIM-BP2 KO. In Fig. 3C,

182 relative amplitudes of Ca^{2+} currents and capacitance in response to a 100 ms pulse are

183 plotted. The RIM-BP2 KO data were superimposed on the WT data. These results confirmed

184 that synaptic vesicles have similar sensitivity to Ca^{2+} influx in both genotypes.

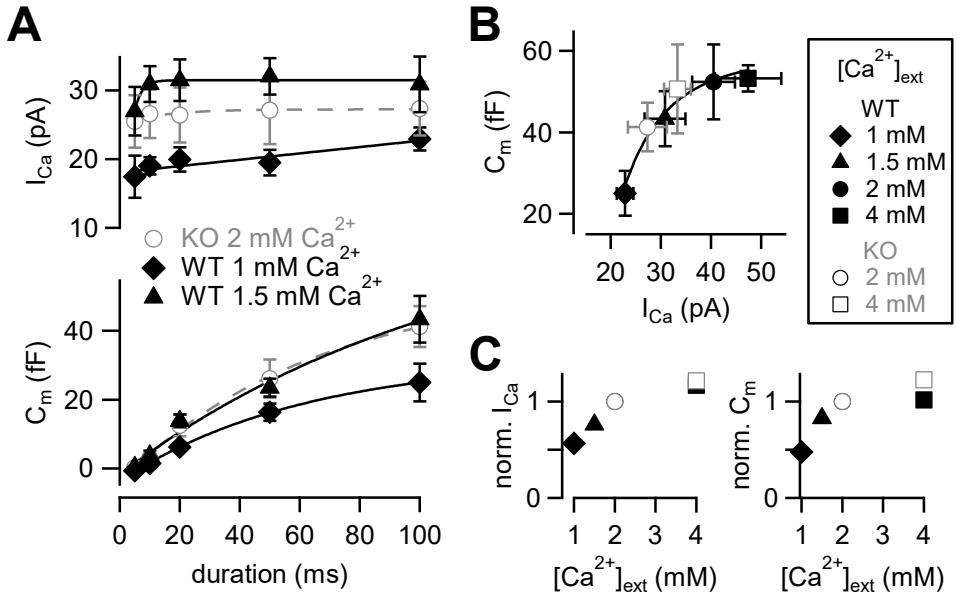

185

186 **Figure 3. Calcium-dependence of the release kinetics and the RRP size**

187 (**A**) *(top)* The relationship between peak Ca^{2+} currents and pulse durations at different

188 $[Ca^{2+}]_{ext}$s. *(bottom)* The relationship between capacitance jumps and pulse durations at

189 different $[Ca^{2+}]_{ext}$s. Gray open circles, black diamonds and black triangles represent the data

190 from RIM-BP2 KO at 2 mM $[Ca^{2+}]_{ext}$ (n = 8) (the same data set as Fig. 1B), WT at 1 mM

191 $[Ca^{2+}]_{ext}$ (n = 3-5) and WT at 1.5 mM $[Ca^{2+}]_{ext}$ (n = 5-7), respectively. Each data point

192 represents mean ± SEM. (**B**) Capacitance jumps at various $[Ca^{2+}]_{ext}$s are plotted against

193 calcium current amplitudes. Pulses were 100 ms depolarization from -80 mV to +10 mV. Each

194 data point represents mean ± SEM. Data points were fitted with a Hill equation with n = 3.

195 (**C**) *(left)* Average I_{Ca}s at indicated $[Ca^{2+}]_{ext}$s were normalized to the response at 2 mM

196 $[Ca^{2+}]_{ext}$ in each genotype. *(right)* Average C_ms at indicated $[Ca^{2+}]_{ext}$s were normalized to the

197 2 mM $[Ca^{2+}]_{ext}$ response in each genotype. Numerical values of plots are provided in Figure

198 3-source data 1.

199 **Source data 1.** Datasets of numerical values presented in Figure 3.

200

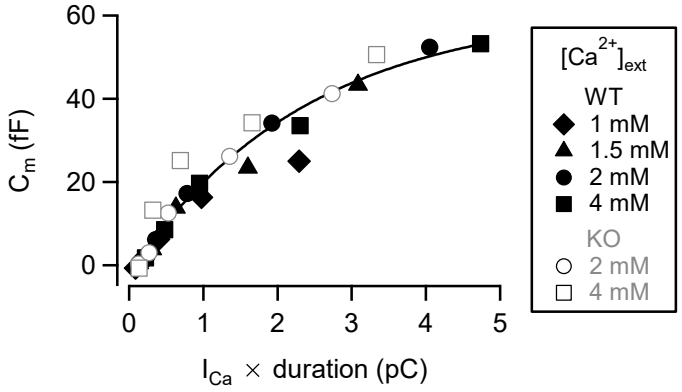

201

202 **Figure 3-figure supplement 1. The relationship between synaptic vesicle release and**

203 **total Ca^{2+} charge**

204 Capacitance jumps elicited by various pulse durations are plotted against total Ca^{2+} charge.

205 The total Ca^{2+} charge is calculated by multiplying a peak Ca^{2+} current amplitude by pulse

206 duration. Each symbol represents a data point obtained from WT (black filled symbols) and

207 RIM-BP2 KO (gray open symbols) mice at various $[Ca^{2+}]_{ext}$. Data points were fitted by a single

208 exponential function. Numerical values of plots are provided in Figure 3-figure supplement

209 1-source data 1.

210 **Figure supplement 1-source data 1.** Datasets of Ca^{2+} charge and ΔC_m presented in Figure

211 3-figure supplement 1.

212

213 **High EGTA experiments suggest unaltered coupling between calcium channels and**

214 **synaptic vesicles.**

215 Previous studies have used Ca^{2+} chelator such as EGTA to examine the sensitivity

216 of release to intracellular Ca^{2+} buffers (Adler et al., 1991; Borst & Sakmann, 1996; Vyleta &

217 Jonas, 2014). When the physical coupling between Ca^{2+} channels and synaptic vesicles is

218 tight, EGTA (slow Ca^{2+} chelator) has less effect on release probability, but EGTA is effective

219 when the coupling is loose. Previous experiments have suggested that RIM-BPs regulate the

220 channel-vesicle coupling at the calyx of Held (Acuna et al., 2015). If this observation also

221 applies to the mossy fiber synapse, EGTA sensitivity of release should be higher in RIM-BP2

222 KO terminals. To investigate the coupling at mossy fiber boutons in RIM-BP2 KO, we

223 changed the concentration of EGTA in the patch pipette. In the presence of 5 mM EGTA, we

224 depolarized the terminal from -80 mV to +10 mV for 5 ms and recorded Ca^{2+} currents and

225 membrane capacitance (Fig. 4A). Ca^{2+} currents and ΔC_m were plotted against pulse duration

226 (Fig. 4B). In both WT and RIM-BP2 KO mice, ΔC_m were reduced under 5 mM EGTA

227 compared with the control condition of 0.5 mM EGTA. We compared the effect of EGTA on
228 average amplitudes of peak Ca^{2+} currents in response to a 20 ms pulse (Fig. 4D).
229 Interestingly, Ca^{2+} current amplitudes were ~1.5 times larger at 5 mM EGTA (53 ± 12 pA, n =
230 5) than at 0.5 mM EGTA (39 ± 3.7 pA, n = 8) in WT, though the data scattered under 5 mM
231 EGTA condition and there was no statistically significant difference (p = 0.524). In RIM-BP2
232 KO, we did not observe such an increase. EGTA might inhibit Ca^{2+} channel inactivation in
233 WT (von Gersdorff and Matthews, 1996). In Fig. 4C, we compared the effect of EGTA on the
234 ΔC_m in response to a 20 ms pulse. In both genotypes, ΔC_m values were inhibited by 5 mM
235 EGTA, and the inhibition was larger in RIM-BP2 KO.

236 Ca^{2+} current amplitudes in RIM-B2 KO are smaller than in WT (Fig. 4B). It is possible
237 that strong effect of high EGTA on release maybe due to reduced Ca^{2+} currents in RIM-BP2
238 KO. Therefore, we changed $[Ca^{2+}]_{ext}$ from 2 mM to 1 mM and adjusted Ca^{2+} current
239 amplitudes of WT to the RIM-BP2 KO level. The capacitance increase and the amplitudes of
240 Ca^{2+} currents became similar to those of RIM-BP2 KO (Fig. 4C and Fig. 4D). These results
241 indicate that WT and RIM-BP2 KO terminals have similar sensitivity of neurotransmitter
242 release to EGTA. Thus, it is unlikely that changes in the coupling distance are responsible
243 for the reduced exocytosis of the mutants.

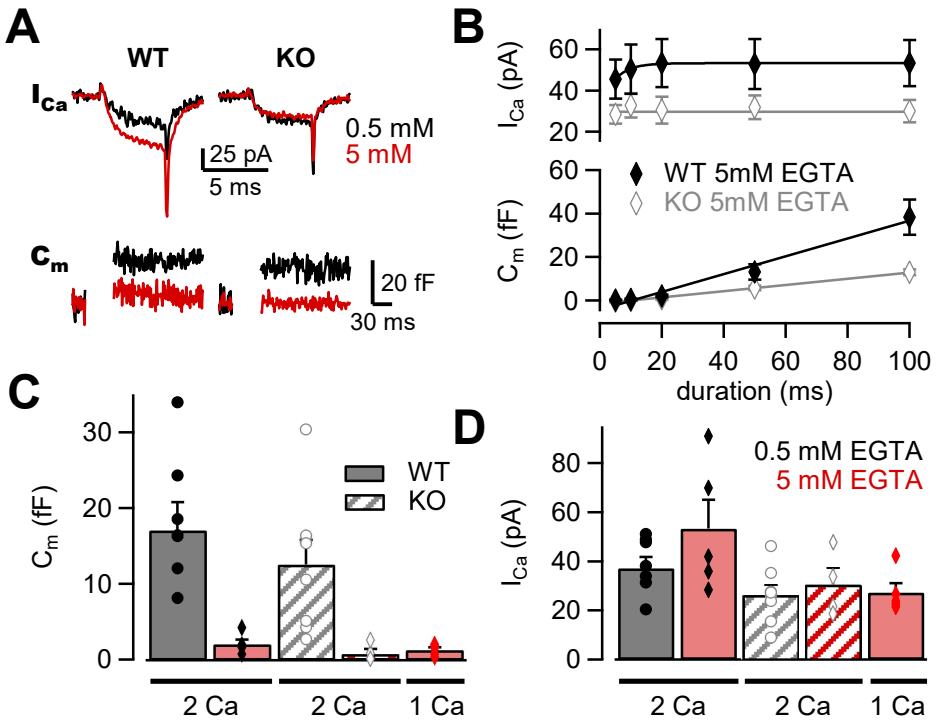

Figure 4. The effects of high EGTA on calcium currents and synaptic vesicle exocytosis

(**A**) Example traces in response to a 5 ms depolarizing pulse to +10 mV in WT *(left)* and RIM-BP2 KO *(right)* boutons. Ca^{2+} current (I_{Ca}) and membrane capacitance (C_m) recorded with 0.5 mM EGTA (black) or 5 mM EGTA (red) in the patch pipette are shown. (**B**) The I_{Ca}s *(top)* and C_ms *(bottom)* are plotted against the pulse duration. The patch pipette contained 5 mM EGTA. Black filled diamonds and gray open diamonds represent the data from WT (n = 4-5) and RIM-BP2 KO (n = 4), respectively. Each data point indicates mean ± SEM. (**C, D**) Average C_ms (**C**) and I_{Ca}s (**D**) elicited by a 20 ms pulse in WT (filled bars) and RIM-BP2 KO (hatched bars). The extracellular Ca^{2+} concentration was 1 mM or 2 mM. The intracellular

255 solution contained either 0.5 mM EGTA (black) or 5 mM EGTA (red). Error bars show SEM.

256 Circles and diamonds indicate individual values. Numerical values of plots are provided in

257 Figure 4-source data 1.

258 **Source data 1.** Datasets of Ca^{2+}-current and capacitance amplitudes presented in Figure 4.

259

260 **STED microscopy reveals that RIM-BP2 KO reduces the density of P/Q-type Ca^{2+}**

261 **channels.**

262 Our electrophysiological data suggest that RIM-BP2 may regulate the density of

263 Ca^{2+} channels, or possibly Ca^{2+} channel properties. In order to directly study the Ca^{2+}

264 channel density at the AZ, we performed STED microscopy analysis of Ca^{2+} channels in WT

265 and RIM-BP2 KO hippocampal mossy fiber terminals. We here focused on P/Q-type and N-

266 type Ca^{2+} channels because both Ca^{2+} channel types are relevant for transmitter release at

267 this synapse (Castillo et al., 1994; Pelkey et al., 2006; Li et al., 2007). We performed

268 immunohistochemistry on thin brain cryosections from WT and RIM-BP2 KO mice. STED

269 microscopy confirmed complete loss of RIM-BP2 proteins in KO terminals (Fig. S2). We then

270 immunohistochemically labeled the α-subunit of either P/Q-type Ca^{2+} channel (Cav2.1) or N-

271 type Ca^{2+} channel (Cav2.2) and Munc13-1 (AZ/release site marker, Böhme et al., 2016;

272 Sakamoto et al., 2018) with VGLUT1 (presynaptic marker) and PSD-95 (postsynaptic

273 marker) (Fig. 5A, Fig. 5B and Fig. S3). In the stratum lucidum of the hippocampal CA3 region,
274 mossy fibers form large synapses containing multiple and clustered AZs on CA3 pyramidal
275 cells, and also small synapses containing a single AZ on interneurons (Acsády et al., 1998;
276 Rollenhagen et al., 2007). Thus, we identified AZs using Munc13-1 STED images and
277 quantified the signal intensity of Cav2.1 or Cav2.2 only at AZs clustered in large VGLUT1
278 positive terminals in the CA3 stratum lucidum, allowing us to confine the analysis to large
279 mossy fiber terminals innervating onto CA3 pyramidal cells. The total signal intensity of
280 Cav2.1 at the AZ was 22% lower in RIM-BP2 KO mice (n = 4 animals) than in WT mice (n =
281 4 animals) (p = 0.0286) (Fig. 5C, left). These data are consistent with the reduction of Ca^{2+}
282 currents in RIM-BP2 KO mice. In contrast to Cav2.1, the total signal intensity of Cav2.2 and
283 Munc13-1 did not significantly differ between WT and RIM-BP2 KOs (p = 0.3143 and p =
284 0.0831) (Fig. 5C, right). Furthermore, we found that the number of Cav2.1 clusters within the
285 AZ identified by STED deconvolution analysis was not altered (2.5 ± 0.11 in WT, n = 4
286 animals; 2.3 ± 0.02 in KO, n = 4 animals) (p = 0.114). These data suggest that RIM-BP2 KO
287 reduces the number of P/Q-type Ca^{2+} channels per cluster. To optically estimate physical
288 distances between Ca^{2+} channels and release sites, we next analyzed the nearest
289 neighboring distance between Cav2.1 and Munc13-1 clusters. These distances were
290 unchanged (61 ± 1.4 nm in WT, n = 4 animals; 64 ± 1.3 nm in KO, n = 4 animals) (p = 0.200)

291 (Fig. 5D), consistent with the similar sensitivity of release to EGTA between WT and RIM-

292 BP2 KO mice. From these results, we conclude that decreased Ca^{2+} influx in RIM-BP2 KO

293 hippocampal mossy fiber terminals is caused by reduction in the density of P/Q-type Ca^{2+}

294 channels at the AZ.

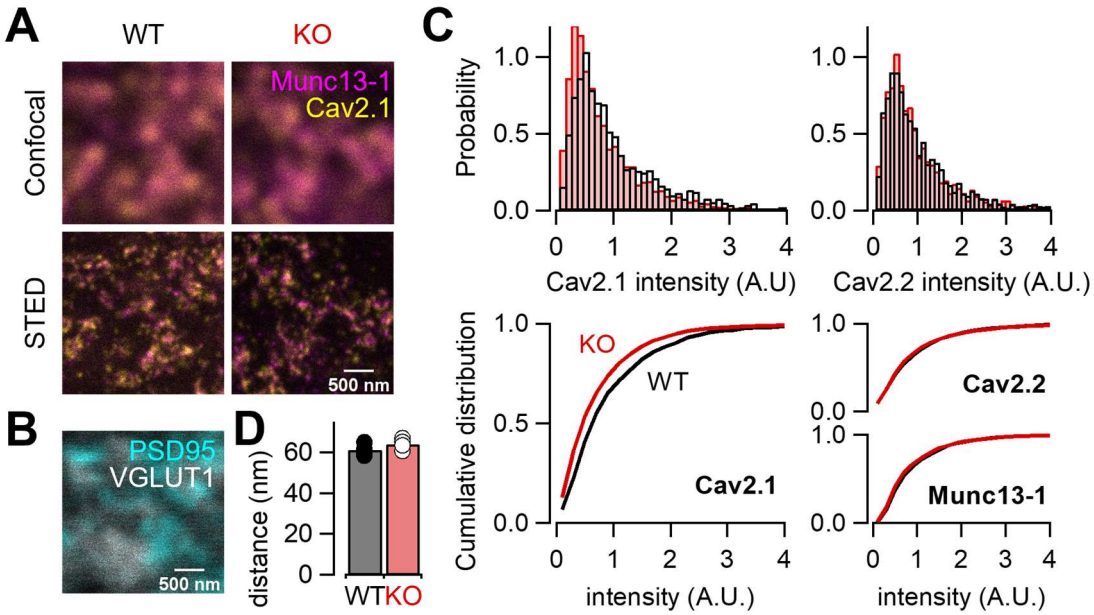

295

296 **Figure 5. RIM-BP2 deletion alters the density of Cav2.1 clusters within the AZ**

297 (**A**) Confocal *(top)* and STED *(bottom)* images of Munc13-1 (magenta) and Cav2.1 (yellow)

298 clusters at hippocampal mossy fiber terminals of WT *(left)* and RIM-BP2 KO *(right)* mice.

299 (Scale bar: 500 nm.) (**B**) Confocal images of PSD95 (cyan) and VGLUT1 (white) to identify

300 glutamatergic synapses in CA3 stratum lucidum: mossy fiber-CA3 synapses. (Scale bar: 500

301 nm.) The image is taken from same region shown in (**A**), *(left)*. (**C**) Histograms *(top)* and

302 cumulative distribution plots *(bottom)* of the total signal intensity of Cav2.1 *(left)*, Cav2.2, and

303 Munc13-1 *(right)* at AZs in WT (black) and RIM-BP2 KO (red) mice. (**D**) The average nearest

304 neighbor distance between Cav2.1 and Munc13-1 clusters in WT (black; n = 4 animals) and

305 RIM-BP2 KO (red; n = 4 animals) mice. Several hundreds of AZs per image were analyzed.

306 Data show the average value of distance per animal and error bars represent SEM. Each

307 data point indicates individual values. Numerical values of plots are provided in Figure 5-

308 source data 1.

309 **Source data 1.** Datasets of numerical values presented in Figure 5.

310

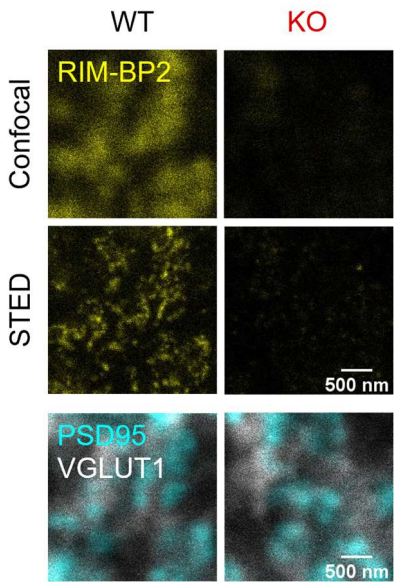

311

312 **Figure 5-figure supplement 1. STED microscopy confirmed loss of RIM-BP2 proteins**

313 **in KO terminals**

314 Confocal *(top)* and STED *(middle)* images of RIM-BP2 (yellow) in WT *(left)* and RIM-BP2 KO

315 *(right)* hippocampal mossy fiber terminals identified by PSD95 (cyan) and VGLUT1 (white)

316 *(bottom)*. (Scale bar: 500 nm.) The *bottom* images show the same region as *top* and *middle*.

317

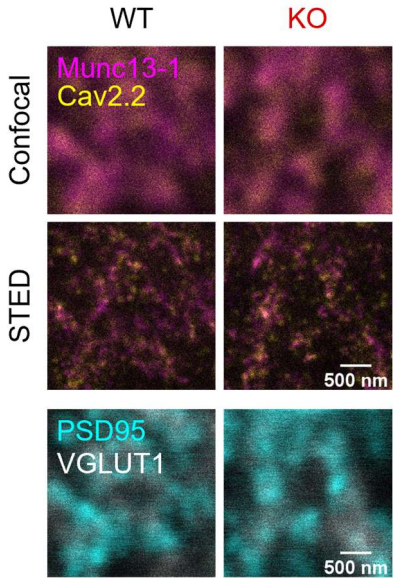

318

319 **Figure 5-figure supplement 2. STED imaging of Cav2.2 at hippocampal mossy fiber**

320 **terminals**

321 Confocal *(top)* and STED *(middle)* images of Munc13-1 (magenta) and Cav2.2 (yellow)

322 clusters in WT *(left)* and RIM-BP2 KO *(right)* mice. Confocal images of PSD95 (cyan) and

323 VGLUT1 (white) in the same region as *top* and *middle* are also shown *(bottom)*. (Scale bar:

324 500 nm.)

325

326 **Discussion**

327 Accumulation of Ca^{2+} channels at the AZ, and efficient vesicle docking and priming

328 are essential factors for fast synaptic vesicle exocytosis. AZ proteins are critical for fast

329 synchronous release and synaptic diversity. RIM-BPs have been implicated in recruitment of
330 Ca^{2+} channels to the AZ (Kaeser et al., 2011; Liu et al., 2011) by interacting with RIMs and
331 Ca^{2+} channels (Wang et al., 2000; Hibino et al., 2002). In addition, RIM-BPs, like RIM1/2,
332 recruit Munc-13 and accelerate synaptic vesicle priming (Brockmann et al., 2020).
333 Concerning the relative importance of RIM-BPs on priming vs Ca^{2+} channel recruitment, we
334 still do know little.

335 At murine central synapses, RIM-BPs deficient synapses demonstrate overall a
336 rather mild decrease in the amounts of transmitter release (Acuna et al., 2015; Grauel et al.,
337 2016; Luo et al., 2017; Krinner et al., 2017; Brockmann et al., 2019; Butola et al., 2021). Most
338 studies so far have been focused on synapses with high release probability (phasic
339 synapses) such as the calyx of Held and CA3-CA1 synapses. This said, at mossy fiber-CA3
340 synapses, KO of RIM-BPs has a strong influence on synaptic transmission (Brockmann et
341 al., 2019). Notably, at mossy fiber-CA3 synapses, release probability is relatively low (tonic
342 synapses). It was unknown whether the reduction of transmitter release at RIM-BP2 KO
343 mossy fiber synapses is due to impaired Ca^{2+} channel recruitment, compromised vesicle
344 docking or priming. Using STED microscopy, Brockmann et al. (2019) suggested that the
345 physical recruitment of Munc13-1 might be an important function of RIM-BP2, though
346 functional demonstration had been lacking.

347 By using direct presynaptic patch clamp recordings, we here observed a decrease
348 of Ca^{2+} current amplitudes (~30%) in RIM-BP2 KO mice (Fig. 1). As the rates of exocytosis
349 steeply depend on Ca^{2+} influx (Dodge and Rahamimoff, 1967), the reduced Ca2+ influx is
350 likely sufficient to explain the slowed release time course at RIM-BP2 KO mossy fiber
351 synapses. Moreover, STED microscopy supported decreased density of P/Q-type Ca^{2+}
352 channels (Cav2.1) in the mutant mossy fiber terminal. Brockmann et al. (2019) observed a
353 reduction of Munc13-1 cluster number and docked vesicles in RIM-BP2 deficient synapses
354 at hippocampal mossy fiber terminals. They identified the terminals by using ZnT3, enriched
355 at mossy fiber (Brockmann et al., 2019; Wenzel et al., 1997). Our STED imaging surprisingly
356 did not detect differences in Munc13-1 cluster number at the AZ between WT and RIM-BP2
357 KO mice. Notably, we analyzed the number of Cav2.1, Cav2.2 and Munc13-1 clusters only
358 within AZs showing direct co-localization with VGLUT1 and PSD-95, which mainly reflects
359 the AZs facing CA3 pyramidal cells rather than the synapses onto interneurons (Acsády et
360 al., 1998; Rollenhagen et al., 2007). Such a difference in areas analyze between previous
361 and our study might explain the difference. Still, our results do not exclude roles of RIM-BP2
362 in synaptic vesicle priming. We however suggest that the reduced Ca^{2+} influx might be more
363 critical here when compared to effects of impaired vesicle priming.
364 Recent studies have reported that RIM-BPs deletion altered Ca^{2+} channel

365 localization and loosened the coupling between Ca^{2+} channels and synaptic vesicles at
366 phasic synapses (Acuna et al., 2015; Grauel et al., 2016; Butola et al., 2021). We investigated
367 the Ca^{2+} channel-vesicle coupling at hippocampal mossy fiber terminals. The sensitivity of
368 release to Ca^{2+} chelator EGTA was not changed between WT and RIM-BP2 KO mice. We
369 also indicated RIM-BP2 KO does not alter the coupling of Ca^{2+} channels to release sites by
370 using STED microscopy.

371 At phasic synapses, deletion of RIM-BP2 affects physical distance between Ca^{2+}
372 channels and synaptic vesicles. In contrast, at hippocampal mossy fiber terminals having low
373 release probability (Vyleta and Jonas, 2014), RIM-BP2 KO decreased the number of P/Q-
374 type Ca^{2+} channels, thereby reducing Ca^{2+} influx and neurotransmitter release. Thus, we
375 hypothesize the specific molecular-architectural and biochemical contributions by RIM-BPs
376 might be of different relevance between phasic and tonic synapses. Brockmann et al. (2020)
377 proposed that RIM-BP2 controls Ca^{2+} channel recruitment and vesicle priming by profound
378 interaction with RIMs and Munc13s. These results have been obtained through studying
379 hippocampal cultures dominated by phasic synapses. It seems possible that the interaction
380 among three protein types is tight at phasic synapses, simply because of high density of
381 these proteins at AZs. Alternatively, one might speculate about additional proteins, different
382 interaction surfaces taken, transsynaptic columns (Tang et al., 2016). Deletion of RIM-BP2

383 does not lead to loss of Ca^{2+} channels themselves and/or vesicle priming due to remaining
384 RIMs, Munc13, and other proteins, which can regulate recruitment of Ca^{2+} channels and
385 synaptic vesicle priming without RIM-BP2. Instead, fine-tuning of release such as
386 synchronization is compromised. We hypothesize that AZ scaffold might be differently built,
387 leading to different consequences when eliminating one component. Hence deletion of RIM-
388 BP2 leads to immediate loss of Ca^{2+} channels and/or vesicle priming. This is in line with the
389 proposal that at tonic synapses, synaptic vesicles are only loosely coupled with Ca^{2+}
390 channels (Vyleta and Jonas, 2014) and vesicles are de-primed under resting conditions (Miki
391 et al., 2016; Neher and Brose, 2018). Future research along this line may lead to an
392 understanding of how fine molecular differences in the AZ scaffolds might orchestrate
393 synaptic diversity.
394

395 **Materials and Methods**

396 **Slice preparation**

397 All animal experiments were conducted in accordance with the guidelines of the
398 Physiological Society of Japan, and were approved by Doshisha University Animal
399 Experiment Committee (A22063, D22063).

400 We used male and female C57BL/6 mice (postnatal days 35-40). WT and RIM-BP2

401 KO mice (Grauel et al., 2016) were deeply anesthetized with isoflurane and decapitated.
402 Their brains were quickly removed and chilled in sherbet-like cutting solution containing (in
403 mM): 87 NaCl, 75 sucrose, 25 $NaHCO_3$, 1.25 NaH_2PO_4, 2.5 KCl, 10 glucose, 0.5 $CaCl_2$ and
404 7 $MgCl_2$ bubbled with 95% O_2 and 5% CO_2 (Hallermann et al., 2003). Hippocampal slices
405 (300 μm thick) were prepared from brains using a vibratome (VT1200S, Leica) in ice-cold
406 cutting solution. After slicing, slices were incubated in cutting solution at 37°C for 30 min, and
407 subsequently kept at room temperature (22-25°C) up to 4 h.
408
409 **Whole-cell recordings**
410 Electrophysiological recordings were performed in a recording chamber filled with
411 the extracellular solution containing (in mM): 125 NaCl, 2.5 KCl, 25 glucose, 25 $NaHCO_3$,
412 1.25 NaH_2PO_4, 0.4 ascorbic acid, 3 myo-inositol, 2 Na-pyruvate, 2 $CaCl_2$ and 1 $MgCl_2$
413 saturated with 95% O_2 and 5% CO_2. In some experiments, the concentration of $CaCl_2$ was
414 changed to 1 mM, 1.5 mM and 4 mM. For membrane capacitance measurements, 1 μM
415 tetrodotoxin (TTX, Wako) was added to block Na^+ channels. Moreover, for recording Ca^{2+}
416 currents, 10 mM TEA-Cl was added to block K^+ channels. Slices were visualized by an
417 upright microscope (BX-51, Olympus). Whole-cell patch-clamp recordings were applied to
418 hippocampal mossy fiber terminals at room temperature. The patch pipettes were filled with

419 the intracellular solution containing (in mM): 135 Cs-gluconate, 20 TEA-Cl, 10 Hepes, 5

420 Na_2-phosphocreatine, 4 MgATP, 0.3 GTP and 0.5 EGTA (pH = 7.2 adjusted with CsOH). In

421 some experiments, the concentration of EGTA was changed to 5 mM. Presynaptic patch

422 pipettes (BF150-86-10, Sutter Instrument) had a resistance of 15-20 MΩ and series

423 resistance (R_s) was 30-70 MΩ. R_s was compensated so that residual resistance was 30-35

424 MΩ. Patch-clamp recordings were performed using an EPC10/3 amplifier (HEKA) in

425 voltage-clamp mode, controlled by Patchmaster software (HEKA). Membrane currents

426 were low-pass filtered at 2.9 kHz and sampled at 20 kHz. Membrane capacitance

427 measurements were performed using an EPC10/3 amplifier in the sine + DC configuration

428 (Gillis, 2000) using Patchmaster software (HEKA). A sine wave (30 mV in amplitude, 1000

429 Hz in frequency) was superimposed on the holding potential of -80 mV. Data were obtained

430 from at least three different WT and RIM-BP2 KO terminals in each set of experiments

431 (biological replicate).

432

433 **Immunostaining**

434 Brains of WT and RIM-BP2 KO mice were quickly removed and transferred to

435 cryomold (Sakura Finetek) filled with tissue freezing medium (Leica). Brains were

436 instantaneously frozen on aluminum block in liquid nitrogen and stored at -80°C. For

437 cryosectioning, frozen brains were kept in cryostat (CM1860, Leica) at −18°C for 30 min.
438 Then, 10 μm-thick sections were sliced and collected on cover glasses (Matsunami glass,
439 25×25 No.1). Sections were quickly fixed by dehydration with a heat blower at 50°C for 1
440 min, and further dehydrated in ethanol for 30 min at -25°C and in acetone for 10 min on ice.
441 After blocking with PBS containing 0.3% BSA at room temperature, sections were
442 incubated with primary antibodies diluted in PBS containing 0.3% BSA: anti-VGLUT1
443 (1:2000, Synaptic Systems, guinea pig polyclonal, RRID:AB_887878), anti-PSD-95 (1:50,
444 NeuroMab, Mouse monoclonal IgG2a, clone K28/43, TC Supernatant, RRID:AB_2877189),
445 anti-Munc13-1 (1:1000, Mouse monoclonal IgG1, clone 11B-10G, Sakamoto et al., 2018),
446 and anti-Cav2.1 (1:400, Synaptic Systems, rabbit polyclonal, RRID:AB_2619841) or anti-
447 Cav2.2 (1:400, Synaptic Systems, Mouse monoclonal IgG2b, clone 163E3,
448 RRID:AB_2619843) or anti-RIM-BP2 (1:200, Mouse monoclonal IgG2b, clone 8-4G,
449 Sakamoto et al., 2022) for 3 hours at room temperature. Afterwards, sections were washed
450 and incubated with fluorescence dye labeled secondary antibodies: DyLight 405 Anti-
451 Guinea Pig IgG (Jackson ImmunoResearch, RRID:AB_2340470), Alexa Fluor 488 (Thermo
452 Fisher Scientific) labeled Anti-Mouse IgG2a (Jackson ImmunoResearch,
453 RRID:AB_2338462), STAR635P (Abberior) labeled Anti-Mouse IgG1 (Jackson
454 ImmunoResearch, RRID:AB_2338461), and Alexa Fluor 594 (Thermo Fisher Scientific)

455 labeled Anti-Rabbit IgG (Jackson ImmunoResearch, RRID:AB_2340585) or Anti-Mouse
456 IgG2b (Jackson ImmunoResearch, RRID:AB_2338463) for 1 hour at room temperature.
457 Sections were post-fixed with 4% PFA in PBS and washed with PBS. Sections were
458 mounted on coverslips using Prolong Glass Antifade Mountant (Thermo Fisher Scientific).
459 The same number of sections were obtained from WT and RIM-BP2 KO brains and
460 processed in parallel at the same experimental day (biological replicate).
461
462 **STED imaging**
463 STED imaging was performed using TCS SP8 STED 3x microscope (Leica)
464 equipped with a 405 nm diode laser, a pulsed white light laser (WLL), a continuous 592 nm
465 STED laser for alignment, a pulsed 775 nm STED laser, HyD detectors, and a 100× oil-
466 immersion objective lens (NA = 1.4). STED images were acquired using the Leica LAS-X
467 software with an image format of 1024×1024 pixels, 16-bit sampling, 8-line accumulations,
468 and 11.36-zoom factor, yielding a pixel size of 10 nm. HyD detectors were configured to
469 counting mode with a gating from 0.5 to 6.5 nanosecond. A 405 nm diode laser was used to
470 excite DyLight405. Alexa488, Alexa594, and STAR635P were excited using WLL at 488
471 nm, 561 nm, and 633 nm, respectively. The 775 nm STED laser power was set to 75% and
472 100% of maximum power for depletion of STAR635P and Alexa594, respectively, and delay

473 time was set to 300 picoseconds. STED imaging was performed on thin sections obtained
474 from four different WT and RIM-BP2 KO mice (biological replicate). Images were acquired
475 three times from each section (technical replicate).
476
477 **Analysis**
478 For electrophysiological experiments, the data were analyzed by Igor Pro
479 (WaveMetrics) or Excel (Microsoft Corp). To determine the time constant of release, an
480 exponential fit was applied. Values are given as mean ± SEM, and n indicates the number
481 of recorded terminals. Statistical method of sample size determination was not done, but
482 our sample sizes are similar to those of previous studies (Hallermann et al., 2003,
483 Midorikawa and Sakaba, 2017).
484 For STED imaging, data were analyzed using custom-designed programs in
485 Mathematica (Wolfram), values were processed by Igor Pro (WaveMetrics), and pictures
486 were created with ImageJ (NIH). To determine the area of AZs, image masks were
487 generated from STED images of Munc13-1 by unsharp masking and image binarization.
488 Only AZs that show co-localization with VGLUT1 and PSD-95 immunofluorescence signals
489 were included in the analysis. To confine the analysis to the large mossy fiber boutons, AZs
490 in presynaptic terminals of small VGLUT1-positive area were excluded. Then, the

491 background subtracted integral of signal intensity of Cav2.1 or Cav2.2 was quantified using
492 the image masks of AZs. The background signal intensity was estimated from non-AZ area
493 in the same STED images. For quantification of Cav2.1 clusters in the AZs, STED images
494 of Cav2.1 were deconvolved using a gaussian kernel with a radius of 40 nm. Image masks
495 of each Ca^{2+} channel were generated from deconvolved STED images by unsharp masking
496 and image binarization. Then, the total signal intensity, the size, and the number of Cav2.1
497 clusters at the AZs were quantified using the image masks of Cav2.1 clusters. Custom-
498 designed programs in Mathematica (Wolfram) are available from Source code 1. Values
499 are given as mean ± SEM, and n indicates the number of animals. Statistical method of
500 sample size determination was not done, but our sample sizes are similar to those of
501 previous studies (Brockmann et al., 2019).
502 Experiments were not fully randomized and blinded.
503 Statistical analysis was done in MATLAB (The MathWorks). To consider the data
504 variability among terminals, Wilcoxon rank sum test was used for significance test of two
505 groups. Significance level was set at $\alpha = 0.05$, and p values were described in the main text
506 or figure legends.
507
508 **Data availability**

All data generated in this study are included in the main text or shown as scatter plots in each graph. Numerical values of graphs are provided in Source data files. The custom-written code files in Mathematica are uploaded as Source code file.

Acknowledgements

We thank Stephan Sigrist, Dietmar Schmitz and Christian Rosenmund for kindly providing us RIM-BP2 KO mice. We also thank Stephan Sigrist for comments on the manuscript and The IRCN Imaging Core, The University of Tokyo Institutes for Advanced Studies, for the use of STED microscopy and for assistance. This works has been supported by JSPS KAKENHI (20J20550 to RM, 20KK0171, 21K15183 to HS, 20H03427 to KH, 20KK0171, 21H02598 to TS), JSPS core-to-core program A, Advanced Research Networks (JPJSCCA2022007 to TS) and JST, PRESTO (JPMJPR21E7 to HS).

Competing interests

None

Additional information

Author ORCIDs

Rinako Miyano https://orcid.org/0000-0002-0022-7198

Hirokazu Sakamoto https://orcid.org/0000-0002-9881-5173

Kenzo Hirose https://orcid.org/0000-0002-8944-6513

Takeshi Sakaba https://orcid.org/0000-0003-0688-7717

532 **References**

533 Acsády L, Kamondi A, Sík A, Freund T, Buzsáki G. 1998. GABAergic cells are the major
534 postsynaptic targets of mossy fibers in the rat hippocampus. *Journal of Neuroscience*
535 **18**:3386-3403. DOI: https://doi.org/10.1523/JNEUROSCI.18-09-03386.1998, PMID:
536 9547246

537 Acuna C, Liu X, Gonzalez A, Südhof TC. 2015. RIM-BPs Mediate Tight Coupling of
538 Action Potentials to Ca^{2+}-Triggered Neurotransmitter Release. *Neuron* **87**:1234-1247.
539 DOI: https://doi.org/10.1016/j.neuron.2015.08.027, PMID: 26402606

540 Adler EM, Augustine GJ, Duffy SN, Charlton MP. 1991. Alien intracellular calcium
541 chelators attenuate neurotransmitter release at the squid giant synapse. *Journal of*
542 *Neuroscience* **11**:1496-1507. DOI: https://doi.org/10.1523/JNEUROSCI.11-06-
543 01496.1991, PMID: 1675264

544 Borst JG, Sakmann B. 1996. Calcium influx and transmitter release in a fast CNS
545 synapse. *Nature* **383**:431-434. DOI: https://doi.org/10.1038/383431a0, PMID: 8837774

546 Brockmann MM, Maglione M, Willmes CG, Stumpf A, Bouazza BA, Velasquez LM, Grauel
547 MK, Beed P, Lehmann M, Gimber N, Schmoranzer J, Sigrist SJ, Rosenmund C, Schmitz
548 D. 2019. RIM-BP2 primes synaptic vesicles *via* recruitment of Munc13-1 at hippocampal
549 mossy fiber synapses. *eLife* **8**:e43243. DOI: https://doi.org/10.7554/eLife.43243, PMID:
550 31535974

551 Brockmann MM, Zarebidaki F, Camacho M, Grauel MK, Trimbuch T, Südhof TC,
552 Rosenmund C. 2020. A Trio of Active Zone Proteins Comprised of RIM-BPs, RIMs, and
553 Munc13s Governs Neurotransmitter Release. *Cell Reports* **32**:107960-107960. DOI:
554 https://doi.org/10.1016/j.celrep.2020.107960, PMID: 32755572

555 Butola T, Alvanos T, Hintze A, Koppensteiner P, Kleindienst D, Shigemoto R, Wichmann
556 C, Moser T. 2021. RIM-Binding Protein 2 Organizes Ca^{2+} Channel Topography and
557 Regulates Release Probability and Vesicle Replenishment at a Fast Central Synapse.
558 *Journal of Neuroscience* **41**:7742-7767. DOI: https://doi.org/10.1523/JNEUROSCI.0586-
559 21.2021, PMID: 34353898

560 Castillo PE, Weisskopf MG, Nicoll RA. 1994. The role of Ca^{2+} channels in hippocampal
561 mossy fiber synaptic transmission and long-term potentiation. *Neuron* **12**:261-269. DOI:
562 https://doi.org/10.1016/0896-6273(94)90269-0, PMID: 8110457

563 Dodge FA, Rahamimoff R. 1967. Co-operative action a calcium ions in transmitter release
564 at the neuromuscular junction. *The Journal of physiology* **193**:419-432. DOI:
565 https://doi.org/10.1113/jphysiol.1967.sp008367, PMID: 6065887

566 Grauel MK, Maglione M, Reddy-Alla S, Willmes CG, Brockmann MM, Trimbuch T,
567 Rosenmund T, Pangalos M, Vardar G, Stumpf A, Walter AM, Rost BR, Eickholt BJ,
568 Haucke V, Schmitz D, Sigrist SJ, Rosenmund C. 2016. RIM-binding protein 2 regulates
569 release probability by fine-tuning calcium channel localization at murine hippocampal
570 synapses. *PNAS* **113**:11615-11620. DOI: https://doi.org/10.1073/pnas.1605256113,
571 PMID: 27671655

572 Hallermann S, Pawlu C, Jonas P, Heckmann M. 2003. A large pool of releasable vesicles
573 in a cortical glutamatergic synapse. *PNAS* **100**:8975-8980. DOI:
574 https://doi.org/10.1073/pnas.1432836100, PMID: 12815098

575 Hibino H, Pironkova R, Onwumere O, Vologodskaia M, Hudspeth AJ, Lesage F. 2002.
576 RIM binding proteins (RBPs) couple Rab3-interacting molecules (RIMs) to voltage-gated
577 Ca^{2+} channels. *Neuron* **34**:411-423. DOI: https://doi.org/10.1016/s0896-6273(02)00667-0,
578 PMID: 11988172

579 Kaeser PS, Deng L, Wang Y, Dulubova I, Liu X, Rizo J, Südhof TC. 2011. RIM proteins
580 tether Ca^{2+} channels to presynaptic active zones via a direct PDZ-domain interaction. *Cell*
581 **144**:282-295. DOI: https://doi.org/10.1016/j.cell.2010.12.029, PMID: 21241895

582 Katz B. 1969. The release of neural transmitter substances. Liverpool University Press.
583 ISBN: 0853230609

584 Krinner S, Butola T, Jung S, Wichmann C, Moser T. 2017. RIM-Binding Protein 2
585 Promotes a Large Number of $Ca_V1.3$ Ca^{2+}-Channels and Contributes to Fast Synaptic
586 Vesicle Replenishment at Hair Cell Active Zones. *Frontiers in Cellular Neuroscience*
587 **11**:334. DOI: https://doi.org/10.3389/fncel.2017.00334, PMID: 29163046

588 Li L, Bischofberger J, Jonas P. 2007. Differential gating and recruitment of P/Q-, N-, and
589 R-type Ca^{2+} channels in hippocampal mossy fiber boutons. *Journal of Neuroscience*

590 **27**:13420-13429. DOI: https://doi.org/10.1523/JNEUROSCI.1709-07.2007, PMID:
591 18057200

592 Lindau M, Neher E. 1988. Patch-clamp techniques for time-resolved capacitance
593 measurements in single cells. *Pflügers Archiv* **411**:137-146. DOI:
594 https://doi.org/10.1007/BF00582306, PMID: 3357753

595 Liu KS, Siebert M, Mertel S, Knoche E, Wegener S, Wichmann C, Matkovic T,
596 Muhammad K, Depner H, Mettke C, Bückers J, Hell SW, Müller M, Davis GW, Schmitz D,
597 Sigrist SJ. 2011. RIM-binding protein, a central part of the active zone, is essential for
598 neurotransmitter release. *Science* **334**:1565-1569. DOI:
599 https://doi.org/10.1126/science.1212991, PMID: 22174254

600 Luo F, Liu X, Südhof TC, Acuna C. 2017. Efficient stimulus-secretion coupling at ribbon
601 synapses requires RIM-binding protein tethering of L-type Ca^{2+} channels. *Proceedings of*
602 *the National Academy of Sciences* **114**:E8081-E8090. DOI:
603 https://doi.org/10.1073/pnas.1702991114, PMID: 28874522

604 Midorikawa M, Sakaba T. 2017. Kinetics of Releasable Synaptic Vesicles and Their
605 Plastic Changes at Hippocampal Mossy Fiber Synapses. *Neuron* **96**:1033-1040.e3. DOI:
606 https://doi.org/10.1016/j.neuron.2017.10.016, PMID: 29103807

607 Miki T, Malagon G, Pulido C, Llano I, Neher E, Marty A. 2016. Actin- and Myosin-
608 Dependent Vesicle Loading of Presynaptic Docking Sites Prior to Exocytosis. *Neuron*
609 **91**:808-823. DOI: https://doi.org/10.1016/j.neuron.2016.07.033, PMID: 27537485

610 Mittelstaedt T, Schoch S. 2007. Structure and evolution of RIM-BP genes: identification of
611 a novel family member. *Gene* **403**:70-79. DOI:
612 https://doi.org/10.1016/j.gene.2007.08.004, PMID: 17855024

613 Müller M, Genç Ö, Davis GW. 2015. RIM-binding protein links synaptic homeostasis to
614 the stabilization and replenishment of high release probability vesicles. *Neuron* **85**:1056-
615 1069. DOI: https://doi.org/10.1016/j.neuron.2015.01.024, PMID: 25704950

616 Neher E, Brose N. 2018. Dynamically Primed Synaptic Vesicle States: Key to Understand
617 Synaptic Short-Term Plasticity. *Neuron* **100**:1283-1291. DOI:
618 https://doi.org/10.1016/j.neuron.2018.11.024, PMID: 30571941

619 Pelkey KA, Topolnik L, Lacaille J-C, McBain CJ. 2006. Compartmentalized Ca^{2+} channel
620 regulation at divergent mossy-fiber release sites underlies target cell-dependent plasticity.
621 *Neuron* **52**:497-510. DOI: https://doi.org/10.1016/j.neuron.2006.08.032, PMID: 17088215

622 Petzoldt AG, Götz TWB, Driller JH, Lützkendorf J, Reddy-Alla S, Matkovic-Rachid T, Liu
623 S, Knoche E, Mertel S, Ugorets V, Lehmann M, Ramesh N, Beuschel CB, Kuropka B,
624 Freund C, Stelzl U, Loll B, Liu F, Wahl MC, Sigrist SJ. 2020. RIM-binding protein couples
625 synaptic vesicle recruitment to release sites. *Journal of Cell Biology* **219**:e201902059.
626 DOI: https://doi.org/10.1083/jcb.201902059, PMID: 32369542

627 Rollenhagen A, Sätzler K, Rodríguez EP, Jonas P, Frotscher M, Lübke JHR. 2007.
628 Structural determinants of transmission at large hippocampal mossy fiber synapses.
629 *Journal of Neuroscience* **27**:10434-10444. DOI:
630 https://doi.org/10.1523/JNEUROSCI.1946-07.2007, PMID: 17898215

631 Sakamoto H, Ariyoshi T, Kimpara N, Sugao K, Taiko I, Takikawa K, Asanuma D, Namiki
632 S, Hirose K. 2018. Synaptic weight set by Munc13-1 supramolecular assemblies. *Nature*
633 *neuroscience* **21**:41–49. DOI: https://doi.org/10.1038/s41593-017-0041-9, PMID:
634 29230050

635 Sakamoto H, Kimpara N, Namiki S, Hamada S, Ohtsuka T, Hirose K. 2022. Synapse type-
636 specific molecular nanoconfigurations of the presynaptic active zone in the hippocampus
637 identified by systematic nanoscopy [unpublished manuscript]. *bioRxiv* 2022.03.11.483942.
638 DOI: https://doi.org/10.1101/2022.03.11.483942

639 Schneggenburger R, Meyer AC, Neher E. 1999. Released fraction and total size of a pool
640 of immediately available transmitter quanta at a calyx synapse. *Neuron* **23**:399-409. DOI:
641 https://doi.org/10.1016/s0896-6273(00)80789-8, PMID: 10399944

642 Südhof TC. 2012. The presynaptic active zone. *Neuron* **75**:11-25. DOI:
643 https://doi.org/10.1016/j.neuron.2012.06.012, PMID: 22794257

644 Tang AH, Chen H, Li TP, Metzbower SR, MacGillavry HD, Blanpied TA. 2016. A trans-
645 synaptic nanocolumn aligns neurotransmitter release to receptors. *Nature* **536**:210-214.
646 DOI: https://doi.org/10.1038/nature19058, PMID: 27462810

647 Thanawala MS, Regehr WG. 2013. Presynaptic calcium influx controls neurotransmitter
648 release in part by regulating the effective size of the readily releasable pool. *Journal of*

649 *Neuroscience* **33**:4625-4633. DOI: https://doi.org/10.1523/JNEUROSCI.4031-12.2013,
650 PMID: 23486937

651 von Gersdorff H, Matthews G. 1996. Calcium-dependent inactivation of calcium current in
652 synaptic terminals of retinal bipolar neurons. *Journal of Neuroscience* **16**:115-122. DOI:
653 https://doi.org/10.1523/JNEUROSCI.16-01-00115.1996, PMID: 8613777

654 Vyleta NP, Jonas P. 2014. Loose coupling between Ca^{2+} channels and release sensors at
655 a plastic hippocampal synapse. *Science* **343**:665-670. DOI:
656 https://doi.org/10.1126/science.1244811, PMID: 24503854

657 Wadel K, Neher E, Sakaba T. 2007. The coupling between synaptic vesicles and Ca^{2+}
658 channels determines fast neurotransmitter release. *Neuron* **53**:563-575. DOI:
659 https://doi.org/10.1016/j.neuron.2007.01.021, PMID: 17296557

660 Wang Y, Sugita S, Südhof TC. 2000. The RIM/NIM family of neuronal C2 domain
661 proteins. Interactions with Rab3 and a new class of Src homology 3 domain proteins.
662 *Journal of Biological Chemistry* **275**:20033-20044. DOI:
663 https://doi.org/10.1074/jbc.M909008199, PMID: 10748113

664 Wenzel HJ, Cole TB, Born DE, Schwartzkroin PA, Palmiter RD. 1997. Ultrastructural
665 localization of zinc transporter-3 (ZnT-3) to synaptic vesicle membranes within mossy fiber
666 boutons in the hippocampus of mouse and monkey. *PNAS* **94**:12676-12681. DOI:
667 https://doi.org/10.1073/pnas.94.23.12676, PMID: 9356509
668